Oblique metal gratings transparent for broadband terahertz waves

Ren-Hao Fan, Jia Li, Ru-Wen Peng, Xian-Rong Huang, Dong-Xiang Qi et al.

Citation: Appl. Phys. Lett. **102**, 171904 (2013); doi: 10.1063/1.4803467
View online: http://dx.doi.org/10.1063/1.4803467
View Table of Contents: http://apl.aip.org/resource/1/APPLAB/v102/i17
Published by the American Institute of Physics.

Oblique metal gratings transparent for broadband terahertz waves

Ren-Hao Fan,[1] Jia Li,[1,2] Ru-Wen Peng,[1,a)] Xian-Rong Huang,[3,a)] Dong-Xiang Qi,[1] Di-Hu Xu,[1] Xiao-Ping Ren,[1] and Mu Wang[1,a)]
[1]*National Laboratory of Solid State Microstructures and Department of Physics, Nanjing University, Nanjing 210093, China*
[2]*Wuhan Institute of Physics and Mathematics, Chinese Academy of Sciences, Wuhan 430071, China*
[3]*Advanced Photon Source, Argonne National Laboratory, Argonne, Illinois 60439, USA*

(Received 25 March 2013; accepted 13 April 2013; published online 30 April 2013)

In this work, we experimentally and theoretically demonstrate that oblique metal gratings with optimal tilt angles can become transparent for broadband terahertz waves under normal incidence. Direct imaging is applied to intuitively prove this broadband transparency phenomenon of structured metals. The transparency is insensitive to the grating thickness due to the non-resonance mechanism, and the optimal tilt angle is determined only by the strip width and the grating period. The oblique metal gratings with broadband transparence may have many potential applications, such as transparent conducting panels, white-beam polarizers, and stealth objects. [http://dx.doi.org/10.1063/1.4803467]

Making metals transparent for electromagnetic waves can lead to a variety of novel applications in optoelectronic devices,[1,2] but unfortunately bulk metals are all naturally opaque to light. Recently, it has been found that structured metals can become transparent via resonance mechanisms.[3–13] For example, free surface electron oscillations driven by the incident wave may excite surface plasmons (SPs)[14] or spoof surface plasmons (SSPs) in the long-wavelength regime,[15] which can give rise to extraordinary optical transmission (EOT) through structured metals.[3–7] Electromagnetically induced transparency (EIT)[10,11] in metamaterials is another example, where sharp resonance induced high transmission arises within a broad absorption line profile. Besides, Fabry-Perot (FP) resonance can also make structured metals transparent at the resonant peaks.[4,8] However, all these transparency phenomena occur only within a narrow bandwidth due to the underlying resonance mechanisms, which is one of the major limitations of plasmonics and metamaterials.

Very recently, it has been demonstrated that one-dimensional metallic gratings can become transparent and completely antireflective for extremely broadband electromagnetic waves under oblique incidence.[16–19] This unusual phenomenon can be explained either by the non-resonant excitation mechanism[16] of SPs or SSPs at microscopic level or equivalently by anomalous impedance-match mechanism.[17] This finding may achieve potential applications, such as transparent conducting panels,[20] white-beam polarizers,[21] and antireflective solar cells.[22] However, the oblique-incidence geometry,[16,17] where the incident angle is usually larger than 45°, is inconvenient for the technological applications. To overcome this drawback, here we instead use oblique metal gratings to achieve *normal-incidence* broadband transparence for electromagnetic waves in the terahertz (THz) region. In particular, we apply THz imaging[23–25] of objects placed behind the oblique metal grating to demonstrate directly broadband transparency, which has not been involved in the previous works on transparent metals yet. With this approach, we not only intuitively display the concept of transparent structured metals but also provide a simple and helpful platform for the THz technology.[23–26] Nowadays the THz technology is widely applied in information and communications technology, biology and medical sciences, homeland security, and so on. Note that although both EOT and EIT phenomena have been observed in THz regime,[27–29] almost all of the experiments were narrow bandwidth of operations, and the thicknesses of metallic films were very limited. In this work, we will theoretically and experimentally demonstrate that oblique metal gratings with optimal tilt angles can become transparent for broadband terahertz waves under normal incidence. And we will also show that this broadband transparency is insensitive to the grating thickness due to the non-resonance mechanism.

The oblique metal grating structure we studied is schematically shown in Fig. 1(a), where d, a, and h denote the grating period, the strip width, and the strip thickness, respectively. The tilt angle of the strips is ϕ, and the incidence angle is θ with respect to the surface normal. The incident wave is of transverse-magnetic (TM) polarization with the magnetic field $\mathbf{H}$ parallel to the strips. We carry out the numerical calculations by using the finite-difference time-domain method[30] (the commercial software package is Lumerical FDTD Solution 8.0.1). Since the metals in the THz region can be considered as perfect conductors, we set the metal's relative permittivity as -1 and conductivity as $1.6 \times 10^7\,\Omega\,\mathrm{m}^{-1}$ in the calculation.

To achieve broadband transparency under normal incidence, the tilt angle ϕ of the oblique metal gratings should be optimized first. Similar to our theoretical analysis in Ref. 16, the optimal tilt angle ϕ_f of the grating can be derived based on the force-balance condition.[18] When the light illuminates the oblique metal grating in Fig. 1(a), the incident electric field $\mathbf{E}_{\mathrm{in}}$ drives the movement of free electrons on the top surface AB and part of the slit wall BP, thus applying

a)Authors to whom correspondence should be addressed. Electronic addresses: rwpeng@nju.edu.cn; xiahuang@aps.anl.gov; and muwang@nju.edu.cn

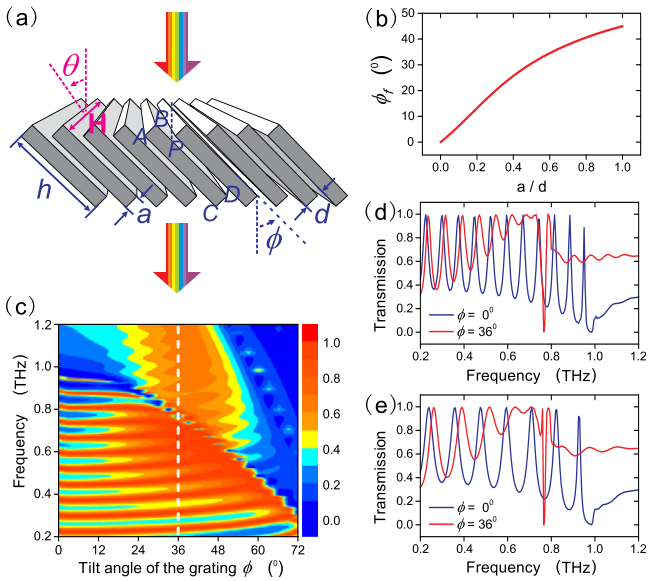

FIG. 1. (a) Schematic of the oblique metal grating. (b) Dependence of the optimal tilt angle (ϕ_f) on the duty cycle (a/d), which is calculated. (c) Calculated normal-incidence ($\theta = 0°$) transmission contour for oblique metal gratings with different tilt angles ϕ. $d = 305\,\mu$m, $a = 200\,\mu$m, and $h = 1.95$ mm. The white dashed line shows the optimal tilt angle determined by Eq. (1). The color bar shows the transmission intensity. (d), (e) Calculated normal-incidence transmission spectra (red curves) for two oblique gratings ($\phi = 36°$) with the same parameters $d = 305\,\mu$m and $a = 200\,\mu$m but with different thicknesses: (d) $h = 1.95$ mm and (e) $h = 1.20$ mm, respectively. For comparison, the blue curves are the corresponding transmission patterns calculated with $\phi = 0°$ (normal gratings with no tilts).

driving forces on the electrons to move on AB and BP. When the total forces exerted on AB and BP are balanced, the electrons can move smoothly around corner B without charge accumulation. Then the charge waves formed on AB and BP may propagate continuously on the unilluminated wall PD to the bottom, resulting in strong light transmission through the slits. The total force applied on the surface AB can be expressed as $F_{AB} = (eE_{\text{in}}\cos\phi)l_{AB}I_{AB}$, where $l_{AB} = a$ is the length of the illuminated surface AB and $I_{AB} \propto \cos\phi$ is the effective photon density that incident on the surface AB. The total force exerts on the illuminated slit wall BP is $F_{BP} = (eE_{\text{in}}\sin\phi)l_{BP}\ I_{BP}$, where $l_{BP} = [(d/\cos\phi) - a\cos\phi]/\sin\phi$ is the length of the illuminated wall BP and $I_{BP} \propto \sin\phi$ is the effective photon density incident on the wall. The balanced-force condition requires $F_{AB} = F_{BP}$, so the optimal tilt angle ϕ_f can be expressed as

$$\tan\phi_f(1 + \tan^2\phi_f)/(1 + \tan\phi_f) = a/d. \qquad (1)$$

The dependence of ϕ_f on the duty cycle a/d given by Eq. (1) is shown in Fig. 1(b), where ϕ_f increases from 0° to 45° when a/d increases from 0 to 1. For $a/d \to 0$, ϕ_f approaches zero, which is consistent with the mechanism of wire grid polarizers.[21] When $a/d \to 1$, a increasingly large ϕ_f is required, leading to a quite oblique grating that, from the ray-tracing viewpoint, seems to be opaque to normal-incidence electromagnetic waves if the grating is thick enough. However, the following numerical calculations and experiments show that the oblique grating is counterintuitively transparent for a wide range of frequencies.

Figure 1(c) shows the calculated transmission spectra of the oblique metal gratings with different tilt angle ϕ, where the grating period, the strip width, and the strip thickness are fixed as $d = 305\,\mu$m, $a = 200\,\mu$m, and $h = 1.95$ mm, respectively. All the data in Fig. 1(c) are collected at normal incidence. Obviously, high broadband transmission indeed occurs through the gratings that have tilt angles around $\phi_f = 36°$ (around the white dashed line), and this optimal angle agrees well with Eq. (1). Figure 1(d) shows more clearly the high normal-incidence transmission (red curve) within the wide low-frequency range, particularly from 0.36 to 0.72 THz. Here some FP resonant peaks still appear,[31,32] but compared with that of the normal gratings with no tilt ($\phi = 0°$, blue curve), the FP resonance effect is significantly suppressed for the grating with $\phi_f = 36°$, leading to a much flatter high-transmission curve in the range from 0.36 to 0.72 THz. Figure 1(e) shows the corresponding transmission curves when the grating thickness is changed to $h = 1.20$ mm, where the transmission pattern for $\phi_f = 36°$ is, on average, similar to that in Fig. 1(d) with $h = 1.95$ mm. This clearly indicates that the broadband transmission phenomenon is dominated by a non-resonant mechanism instead of the thickness-dependent FP resonance mechanism.

We have used steel gratings to experimentally verify the above results. In our experiments, the gratings were assembled with steel strips with dimensions 200 μm $\times$ 1.95 mm $\times$ 6 cm. For comparison, we made two types of steel gratings with tilt angles $\phi = 0°$ and $\phi = 36°$, respectively, as shown in Figs. 2(a) and 2(d). The transmission measurements were carried out with a THz real-time spectrometer (EKSPLA/THz, Lithuania). By scanning the delay line, we obtained the time-domain signal $E(t)$ of the polychromatic THz pulse transmitted through the samples. Afterwards, the transmission spectrum was obtained from the Fourier transform of $E(t)$ within the 0.2–1.2 THz frequency range and normalized with respect to the transmission spectrum of air.

Figures 2(c) and 2(f) show the fine measurements of the optical transmission spectra for the incidence angle θ from $-72°$ to 72° (with 1° step). For the normal grating ($\phi = 0°$), the first-order Wood's anomaly occurs at $f_{\text{WD1}}(\theta) = (c\cos\phi)/d(1 + \sin\theta)$, which is marked by the white dashed line in Fig. 2(c). Nearly, flat high transmission for frequency $f < f_{\text{WD1}}(\theta_f)$ can be observed when the incident angle is around $\theta_f \approx \arctan[a/(d-a)] \approx 62°$, which reasonably agrees with the numerical calculations in Fig. 2(b) and also with the theoretical prediction in Ref. 16. Obviously, this large incident angle is inconvenient for practical applications. As shown in Figs. 2(e) and 2(f), however, the oblique grating can still achieve similar broadband high transmission under the more favorable normal-incidence condition $\theta = 0°$. For example, in Figs. 2(e) and 2(f) the normal-incidence transmission of the oblique grating can reach 80% within the wide band of 0.36–0.72 THz, which presents a nearly flat high transmission zone for the THz waves. As mentioned above, within this zone, the FP resonance is significantly (although not completely) suppressed, and the average normal-incidence transmission intensity is obviously enhanced compared with that of the normal grating under $\phi = 0°$.

The mechanism underlying the broadband high transmission for normal incidence can be understood at microscopic

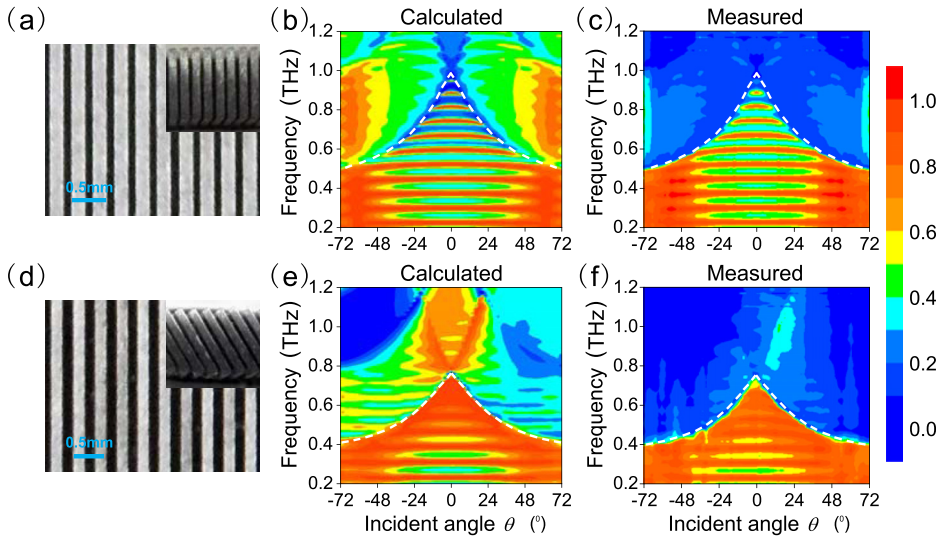

FIG. 2. (a) Photograph of the normal steel grating without tilt ($\phi = 0°$). Insert shows the cross section. (b) Calculated and (c) measured transmission spectra of the sample in (a). (d) Photograph of the oblique steel grating with $\phi = 36°$. (e) Calculated and (f) measured transmission spectra of the sample in (d). Here the incident angle θ ranges from $-72°$ to $72°$ with the sign only indicating the relative incidence direction. The white dashed lines correspond to the first-order Wood's anomalies. Color bar shows the transmission intensity. $d = 305\ \mu$m, $a = 200\ \mu$m, and $h = 1.95$ mm.

level. In a normal grating ($\phi = 0°$), the incident electric field $\mathbf{E}_{in}$ drives the movement of free electrons on the surface AB and CD to form two oscillating dipoles, and they eventually form FP resonance peaks under the condition $m\lambda \approx 2h$, where $m > 0$ is an integer and λ is the wavelength of the incident light. Based on the electric field ($|\mathbf{E}|^2$) distribution at one of FP resonant peak ($f = 0.37$ THz, shown in Fig. 3(a)), one can see that a standing wave is inside the slits and high electric fields are concentrated at the edges of surfaces AB and CD. But in the oblique grating ($\phi = 36°$), the electrons can move smoothly around corner B without charges accumulation under the balanced-force condition, so the FP resonance does not occur, and the electrons move continuously on the entire surfaces AB and BD, which finally leads to non-resonance high transmission through the slits. This non-resonance mechanism is verified from the electric field ($|\mathbf{E}|^2$) distribution at high transmission bandwidth (for example, to see Fig. 3(b) at the same frequency $f = 0.37$ THz), where the electric field intensity is very low and nearly uniform inside the slits. Figure 3(b) indicates that no standing waves exist, and the FP resonance is significantly suppressed in the oblique grating. Therefore, the high-transmission process is insensitive to the grating thickness. Actually the electric field is very weak at corner B, but it becomes sufficiently strong at the corners A and D, which further proves that the balanced-force condition is satisfied for this oblique grating with $\phi = 36°$.

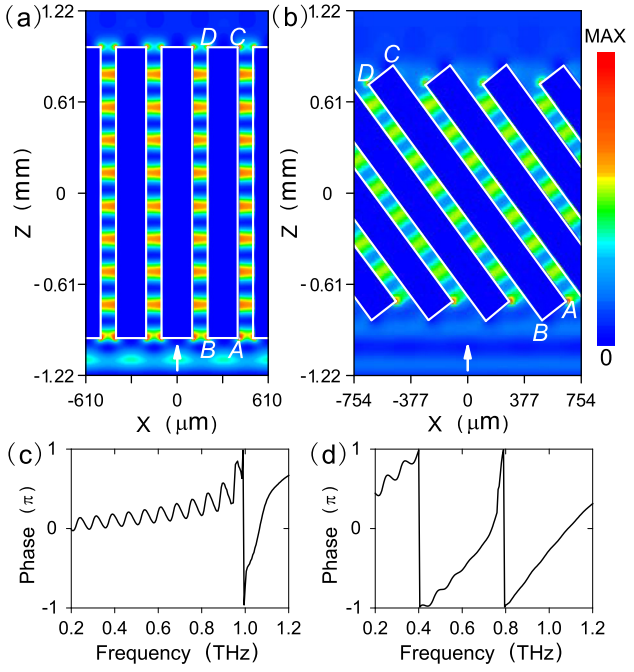

FIG. 3. Calculated $|\mathbf{E}|^2$ distributions of the normal steel grating with $\phi = 0°$ (a) and the oblique grating with $\phi = 36°$ (b) at frequency $f = 0.37$ THz; color bar shows the electric field intensity. Phase shifts of the transmitted waves as functions of the frequency for the normal grating (c) and the oblique grating (d) with respect to the free propagation wave. $d = 305\ \mu$m, $a = 200\ \mu$m, and $h = 1.95$ mm. Normal incidence.

The phase shifts of the transmitted waves with respect to the free propagating wave are also quite different between the two gratings. In Fig. 3(c), the phase shift of the THz wave transmitted through the normal grating dramatically changes around $f_{WD1} = 0.98$ THz, the first-order Wood's anomaly. For lower frequencies, the phase shift slightly oscillates with the

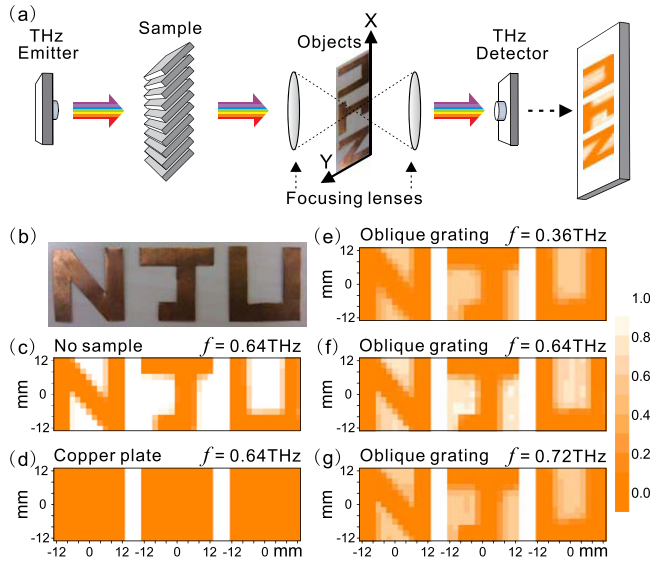

FIG. 4. (a) Schematic of the THz imaging system. (b) Photograph of the objects for imaging. (c) Detected images with no grating before the objects, $f = 0.64$ THz. (d) Blank images with a 0.2 mm-thick copper plate placed at the "sample" position, $f = 0.64$ THz. (e)–(f) Images recorded with an oblique steel grating ($d = 305\ \mu$m, $a = 200\ \mu$m, $h = 1.95$ mm, and $\phi = 36°$) at the "sample" position for different frequencies: (e) $f = 0.36$ THz, (f) $f = 0.64$ THz, and (g) $f = 0.72$ THz. Color bar shows the transmission intensity.

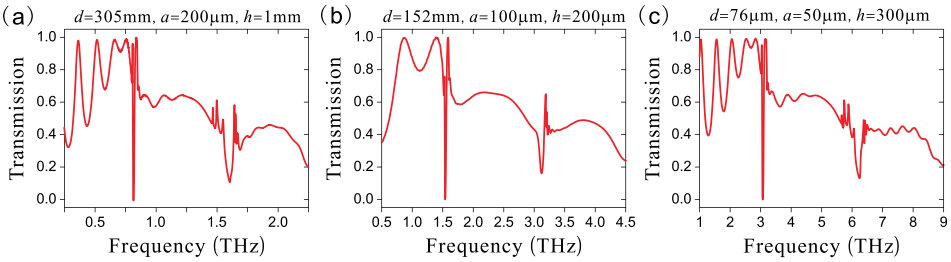

FIG. 5. Variation of the normal-incidence transmission spectra of oblique steel gratings with grating periods d and other parameters. Calculations are based on a fixed tilt angle $\phi = 36°$ and other variable parameters: (a) $d = 305\,\mu$m, $a = 200\,\mu$m, and $h = 1$ mm; (b) $d = 152\,\mu$m, $a = 100\,\mu$m, and $h = 200\,\mu$m; and (c) $d = 76\,\mu$m, $a = 50\,\mu$m, and $h = 300\,\mu$m.

frequency. Here the minimum phase shifts correspond to FP resonance peaks. For the oblique grating in Fig. 3(d), the phase shift also dramatically changes around the first Wood's anomaly, which is $f_{WD1} = 0.80$ THz for this grating. In the lower frequency range from 0.4 to 0.8 THz, however, the phase shift has no obviously oscillation, which again indicates that the FP resonance is significantly suppressed.

The high broadband transmission of oblique gratings can also be directly visualized by THz imaging techniques. As schematically shown in Fig. 4(a), our imaging experiments were carried out with the THz real-time spectrometer. The TM-polarization polychromatic THz pulses are transmitted through the sample before being focused onto the objects for imaging. Here the polyethylene focusing lenses have a focal length of 5.0 cm, and the objects are mounted on a computer-controlled X-Y stage and can be continuously scanned by the focused beam to generate 2D images at selected frequencies. In our experiments, the objects for imaging are three letters "N," "J," and "U" shown in Fig. 4(b), which were made from 0.2 mm-thick copper plates that are completely opaque to the THz beam. In the current experiments, each 2D image we observed consists of 169 pixels, and higher resolution can be obtained by moving the X-Y stage with a smaller step.

We have collected the images of the objects (the letters "N," "J," and "U" in Fig. 4(b)) in the following cases: (i) No samples are before the objects. Figure 4(c) shows the detected 2D images at frequency $f = 0.64$ THz. Naturally, the images in Fig. 4(c) clearly show the three-letter pattern ("NJU"), and the color in the pattern illustrates obvious contrast of the transmission intensity, where dark-colored areas corresponds to low transmission and bright-colored areas to high transmission. The signal-to-noise ratio (SNR), which is defined as the maximum transmission intensity to the average noise intensity, can reach 97:1 at $f = 0.64$ THz. (ii) A homogeneous 0.2-thick copper plate as the sample is placed before the objects. The 2D images are detected at the same frequency $f = 0.64$ THz (as shown in Fig. 4(d)). Obviously no patterns are observed on the images because the THz pulse cannot transmit through the copper plate. (iii) Our oblique steel grating ($\phi = 36°$) as the sample is placed before the objects. The 2D images are detected at the frequency $f = 0.36$ THz, 0.64 THz, and 0.72 THz, respectively (as shown in Figs. 4(e)–4(g)). It is shown that the pattern "NJU" of the objects is displayed very well in all three 2D images. The SNR of 2D images is significantly high. For example, it reaches 83:1 at frequency $f = 0.64$ THz (Fig. 4(f)), which is comparable to the 2D images in Fig. 4(c) at the same frequency. The qualities of the 2D images at $f = 0.36$ THz and $f = 0.72$ THz (as shown in Figs. 4(e) and 4(g)) are also very impressive, and their SNRs can reach 55:1 and 56:1, respectively. Therefore, the 2D images clearly reveal the broadband transparency feature of the oblique metal gratings in the THz region.

Finally, it is worthy to note that the band range for high transmission in oblique metal gratings can be tuned by adjusting the grating periods. For example, by decreasing the grating period d, the high-transmission band of the oblique metal gratings can be tuned from 0.36–0.72 THz in Fig. 5(a) to 0.72–1.44 THz in Fig. 5(b), and further to 1.44–2.88 THz in Fig. 5(c). This tunable feature implies that oblique metal grating can achieve broadband transparence not only for terahertz waves but also for the electromagnetic waves in other frequency regions. In fact, Figure 5 also indicates the multiple-band transmission features. In addition to the low-frequency band ($f < f_{WD1}$) in which the average transmission efficiency can reach about 90%, the high-frequency bands still retains significant transmission although the efficiency relatively decreases due to the non-evanescent diffraction effect.[32]

In summary, we have demonstrated that oblique metal gratings with optimal tilt angle can become transparent for broadband terahertz waves under normal incidence, and the optimal tilt angle is only determined by the duty cycle of the grating. This phenomenon originates from the non-resonance mechanism, where FP resonances are significantly suppressed. Further, the THz imaging has directly shown these structured metals transparent for broadband THz waves. This transparency is insensitive to the grating thickness, and the band range for transparency can be tuned by the grating period. The oblique gratings may have various potential applications on transparent conducting panels, white-beam polarizers, stealth objects, and so on, and the associated non-resonant mechanisms may also shed light on the development of broadband metamaterials.

This work was supported by the Ministry of Science and Technology of China (Grant Nos. 2012CB921502 and 2010CB630705), the National Science Foundation of China (Grant Nos. 11034005, 61077023, and 11021403), and partly by the Ministry of Education of China (20100091110029). X.R.H. was supported by the U.S. Department of Energy, Office of Science, Office of Basic Energy Sciences, under Contract No. DE-AC02-06CH11357.

[1]J. Y. Lee, S. T. Connor, Y. Cui, and P. Peumans, Nano Lett. **8**, 689 (2008).
[2]D. S. Hecht, L. Hu, and G. Irvin, Adv. Mater. **23**, 1482 (2011).
[3]T. W. Ebbesen, H. J. Lezec, H. F. Ghaemi, T. Thio, and P. A. Wolff, Nature (London) **391**, 667 (1998).
[4]J. A. Porto, F. J. García-Vidal, and J. B. Pendry, Phys. Rev. Lett. **83**, 2845 (1999).

[5]Z. H. Tang, R. W. Peng, Z. Wang, X. Wu, Y. J. Bao, Q. J. Wang, Z. J. Zhang, W. H. Sun, and M. Wang, Phys. Rev. B **76**, 195405 (2007).
[6]H. Liu and P. Lalanne, Nature (London) **452**, 728 (2008).
[7]Y. J. Bao, R. W. Peng, D. J. Shu, M. Wang, X. Lu, J. Shao, W. Lu, and N. B. Ming, Phys. Rev. Lett. **101**, 087401 (2008).
[8]J. T. Shen, P. B. Catrysse, and S. Fan, Phys. Rev. Lett. **94**, 197401 (2005).
[9]I. R. Hooper, T. W. Preist, and J. R. Sambles, Phys. Rev. Lett. **97**, 053902 (2006).
[10]S. Zhang, D. A. Genov, Y. Wang, M. Liu, and X. Zhang, Phys. Rev. Lett. **101**, 047401 (2008).
[11]N. Liu, L. Langguth, T. Weiss, J. Kästel, M. Fleischhauer, T. Pfau, and H. Giessen, Nat. Mater. **8**, 758 (2009).
[12]Z. Y. Song, Q. He, S. Y. Xiao, and L. Zhou, Appl. Phys. Lett. **101**, 181110 (2012).
[13]J. D. Edmunds, M. J. Lockyear, A. P. Hibbins, J. R. Sambles, and I. J. Youngs, Appl. Phys. Lett. **102**, 011120 (2013).
[14]W. L. Barnes, A. Dereux, and T. W. Ebbesen, Nature (London) **424**, 824 (2003).
[15]J. B. Pendry, L. Martín-Moreno, and F. J. Garcia-Vidal, Science **305**, 847 (2004).
[16]X. R. Huang, R. W. Peng, and R. H. Fan, Phys. Rev. Lett. **105**, 243901 (2010).
[17]A. Alù, G. D'Aguanno, N. Mattiucci, and M. J. Bloemer, Phys. Rev. Lett. **106**, 123902 (2011).
[18]R. H. Fan, R. W. Peng, X. R. Huang, J. Li, Y. Liu, Q. Hu, M. Wang, and X. Zhang, Adv. Mater. **24**, 1980 (2012).
[19]N. Aközbek, N. Mattiucci, D. de Ceglia, R. Trimm, A. Alù, G. D'Aguanno, M. A. Vincenti, M. Scalora, and M. J. Bloemer, Phys. Rev. B **85**, 205430 (2012).
[20]G. Subramania, S. Foteinopoulou, and I. Brener, Phys. Rev. Lett. **107**, 163902 (2011).
[21]P. Yeh, Opt. Commun. **26**, 289 (1978).
[22]H. A. Atwater and A. Polman, Nat. Mater. **9**, 205 (2010).
[23]K. J. Siebert, H. Quast, R. Leonhardt, T. Löffler, M. Thomson, T. Bauer, H. G. Roskos, and S. Czasch, Appl. Phys. Lett. **80**, 3003 (2002).
[24]J. F. Federici, B. Schulkin, F. Huang, D. Gary, R. Barat, F. Oliveira, and D. Zimdars, Semicond. Sci. Technol. **20**, S266 (2005).
[25]H. B. Liu, H. Zhong, N. Karpowicz, Y. Chen, and X. C. Zhang, Proc. IEEE **95**, 1514 (2007).
[26]N. Krumbholz, K. Gerlach, F. Rutz, M. Koch, R. Piesiewicz, T. Kürner, and D. Mittleman, Appl. Phys. Lett. **88**, 202905 (2006).
[27]F. Miyamaru and M. Hangyo, Appl. Phys. Lett. **84**, 2742 (2004).
[28]E. Hendry, M. J. Lockyear, J. Gómez Rivas, L. Kuipers, and M. Bonn, Phys. Rev. B **75**, 235305 (2007).
[29]R. Singh, C. Rockstuhl, F. Lederer, and W. Zhang, Phys. Rev. B **79**, 085111 (2009).
[30]A. Taflove and S. C. Hagness, *Computational Electrodynamics: The Finite-Difference Time-Domain Method*, 3rd ed. (Artech House, Norwood, 2005).
[31]H. E. Went, A. P. Hibbins, J. R. Sambles, C. R. Lawrence, and A. P. Crick, Appl. Phys. Lett. **77**, 2789 (2000).
[32]X. R. Huang and R. W. Peng, J. Opt. Soc. Am. A **27**, 718 (2010).